Degrees of Freedom in Multiple-Antenna Channels: A Signal Space Approach

Ada S. Y. Poon, Robert W. Brodersen and David N. C. Tse
Berkeley Wireless Research Center
Department of Electrical Engineering and Computer Sciences
University of California, Berkeley
{sypoon, rb, dtse}@eecs.berkeley.edu

28th August 2003

Abstract

We consider multiple-antenna systems that are limited by the area and geometry of antenna arrays. Given these physical constraints, we determine the limit to the number of spatial degrees of freedom available and find that the commonly used statistical multi-input multi-output model is inadequate. Antenna theory is applied to take into account the area and geometry constraints, and define the spatial signal space so as to interpret experimental channel measurements in an array-independent but manageable description of the physical environment. Based on these modeling strategies, we show that for a spherical array of effective aperture $\mathcal{A}$ in a physical environment of angular spread $|\Omega|$ in solid angle, the number of spatial degrees of freedom is $\mathcal{A}|\Omega|$ for unpolarized antennas and $2\mathcal{A}|\Omega|$ for polarized antennas. Together with the $2WT$ degrees of freedom for a system of bandwidth W transmitting in an interval T, the total degrees of freedom of a multiple-antenna channel is therefore $4WT\mathcal{A}|\Omega|$.

1 Introduction

In multiple-antenna channels, the channel capacity grows linearly with the number of spatial degrees of freedom, which is therefore a key performance measure. A fundamental question arises: given an *area* limitation on the transmit and receive antenna arrays, what is the intrinsic number of degrees of freedom available in the channel? Statistical multi-input multi-output (MIMO) models are insufficient to answer this question. Early results [1, 2] focus on

the model where the fading is i.i.d. across all antenna pairs, and show that the number of degrees of freedom is the minimum of the number of transmit and receive antennas. Packing more antennas in a given area will, however, make the fading correlated and therefore cannot increase the capacity indefinitely. This is analogous to the waveform channel where given the bandwidth constraint W and transmission interval T, increasing the number of time samples will also not increase the capacity indefinitely. The available degrees of freedom is fundamentally limited to $2WT$. In this paper, we will demonstrate that the physical constraints of antenna arrays and propagation environment put forth a deterministic limit to the spatial degrees of freedom underlying the statistical MIMO approach.

Let us review the reasoning involved to derive the $2WT$ formula [3, Ch. 8]. In waveform channels, the transmit and receive signals are represented either in the time domain as waveforms or in the frequency domain as spectra. The mapping between these two representations is the Fourier transform. The waveform is then approximately time-limited to $[-T/2, T/2]$ and its spectrum is frequency-limited to $[-W, W]$. The dimension of the subspace satisfying these two physical constraints gives the number of degrees of freedom, $2WT$. To demonstrate an analogous result for multiple-antenna channels, the corresponding spatial signal domains and the mappings between them are required which is based on electromagnetic theory considerations.

In this paper, we incorporate antenna theory with experimental channel modeling to obtain a mathematical model that allows us to derive a more fundamental limit to the spatial degrees of freedom given a constraint on the areas of the transmit and receive antenna arrays. Physically, there are two signal domains of interest: the *array domain* used to describe the excitation current distributions and the *wavevector domain* (also known as *angular domain*) to describe the radiated field patterns. The mapping between them depends on the geometry of the antenna array as it imposes different boundary conditions on the set of Maxwell equations. In the case of linear arrays, the mapping between the array and wavevector domains is the familiar Fourier transform, same as the time/frequency counterparts. The mappings for circular and spherical arrays are however different. The current distribution (in array domain) is then limited by the size of the antenna array while the scattering of the physical environment limits the amount of radiated field (in wavevector or angular domain) reaching the receiver. In the urban and indoor environments, transmitter-receiver separation is typically comparable to the size of channel objects, so propagation paths are no longer discrete but are more appropriately analyzed as clusters, as illustrated in Figure 1. The scattering in the physical environment is then characterized by the number of these clusters and the solid angles subtended. We will show that for a spherical array of effective aperture $\mathcal{A}$ in an environment with scattering clusters spanning over a total solid angle of $|\Omega|$, the number of degrees of freedom is $\mathcal{A}|\Omega|$. When polarization is taken into account, the signal

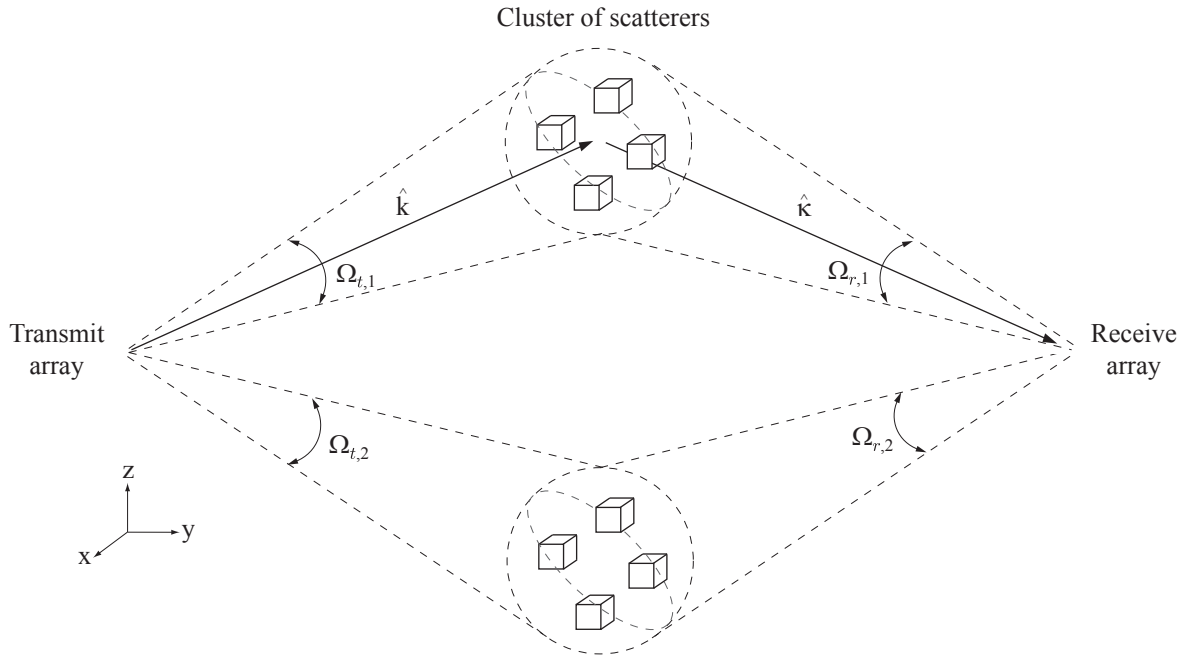

Figure 1: Illustrates the clustering of transmitted and received signals. The scattering intervals are $\Omega_t = \Omega_{t,1} \cup \Omega_{t,2} \cup \cdots$ and $\Omega_r = \Omega_{r,1} \cup \Omega_{r,2} \cup \cdots$.

space becomes a set of vector fields. The number of degrees of freedom is shown to be $2\mathcal{A}|\Omega|$.

The degree-of-freedom formula gives insight on the number of antennas that should be put on the given transmit and receive areas so as to optimize the trade-off between capacity and cost. As the number of RF/analog chains scales linearly with the number of antennas and the complexity in digital baseband increases at least quadratically [4, 5], it is of great incentive to use the optimal number of antennas given the physical environment and the shape of wireless device. We will ascertain that $2\mathcal{A}|\Omega|$ number of antennas suffices.

In addition, the wavevector domain provides an appropriate coordinate to describe the physical position of other users. Extending the mathematical model to multiuser environments is straightforward. If the users are cooperative and relay signals, the channel solid angles will likely increase and so does the spatial degrees of freedom. On the other hand, if the users are non-cooperative and create interference instead, it can be encapsulated as a decrease in the channel solid angles. It turns out that the optimal number of antennas is different in both channels.

Recent works such as [6, 7, 8] also bring in the array and wavevector domains as a mean to relate the scattering of physical environment to the fading correlation among antennas on unpolarized linear arrays. In [6], the physical environment is characterized by the number of propagation paths in the wavevector domain, and the spatial degrees of freedom is the minimum of the numbers of propagation paths, transmit antennas and receive antennas.

Though the number of propagation paths that can be resolved, depends on the area of the transmit and receive arrays, [6] does not take this into account. Therefore, it does not answer our question of number of degrees of freedom per unit area. In [7, 8], the physical environment is also modeled as clusters but in a statistical manner. The decrease in fading correlation with increasing antenna spacing is investigated. It gives an intuitive explanation on how the capacity of linear arrays increases with increasing antenna spacing in different scattering environments. However, if the transmit and receive areas are constrained, then increasing the antenna spacing will reduce the number of antennas and hence will likely decrease the capacity. It is this physical constraint that is the focus of this paper. Furthermore, we use a deterministic signal space approach to look at the scattering in physical environments instead of statistical approaches.

Finally, we have applied the mathematical model to study the degrees of freedom on linear arrays in [9]. Independent works such as [10, 11, 12] also consider the physical constraint of antenna arrays. The first two use statistical approaches while the latter focuses on channel modeling for numerical analysis.

The paper is organized as follows. Section 2 presents the system model. Section 3 derives the spatial degrees of freedom. Section 4 elaborates the physical insight of the main results. Section 5 extends the model from point-to-point to multiuser environments. Section 6 elucidates the optimal number of antennas. Finally, we will conclude this paper in Section 7.

The following notation will be used in this paper. We will use boldface calligraphic letters for electromagnetic entities ($\boldsymbol{\mathcal{E}}, \boldsymbol{\mathcal{J}}, \cdots$), boldface capital letters for matrices ($\mathbf{C}, \mathbf{H}, \cdots$) and boldfaced small letters for vectors ($\mathbf{p}, \mathbf{q}, \cdots$). For a given vector $\mathbf{p}$, $\hat{\mathbf{p}}$ is a unit vector denoting its direction and p denotes its magnitude. i denotes square root of -1. $\nabla_{\mathbf{p}}\times$ denotes the curl operation with respect to $\mathbf{p}$. $\mathbf{I}$ is the identity matrix. $(\cdot)^*$, $(\cdot)^\dagger$ and $\mathsf{E}[\cdot]$ denote conjugate, conjugate-transpose and expectation operations respectively. For a set $\mathcal{S}$, $|\mathcal{S}|$ denotes its Lebesgue measure. $\Re^n$, $\mathcal{C}^n$ and $\mathcal{C}^{n\times m}$ denote the set of n-dimensional real numbers, n-dimensional complex numbers and $n \times m$ complex matrices. $\lceil x \rceil$ gives the smallest interger equal to or greater than x. $(x)^+$ denotes $\max\{0, x\}$.

2 System Models

We consider continuous arrays which are composed of an infinite number of antennas separated by infinitesimal distances. This eliminates the need to specify a prior the number of antennas and their relative positions on the arrays. Each antenna is composed of three orthogonal dipoles oriented along Euclidean directions $\hat{\mathbf{e}}_1$, $\hat{\mathbf{e}}_2$ and $\hat{\mathbf{e}}_3$ as pictured in Figure 2. This antenna topology is often referred as a tripole where arbitrarily polarized electric fields

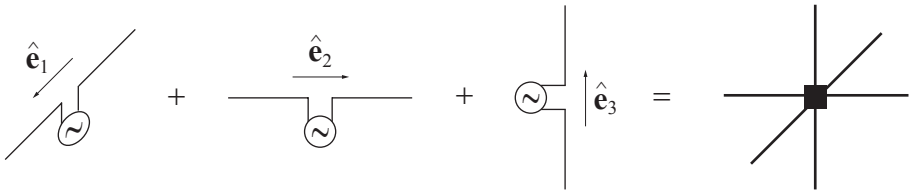

Figure 2: A tripole antenna.

can be generated. In a frequency non-selective fading channel, the transmit and receive signals at a particular time are related by

$$\mathbf{y}(\mathbf{q}) = \int \mathbf{C}(\mathbf{q},\mathbf{p})\,\mathbf{x}(\mathbf{p})\,d\mathbf{p} + \mathbf{z}(\mathbf{q}) \tag{1}$$

The transmit signal $\mathbf{x}(\cdot)$ is a vector field on $\mathcal{R}^3$, a function that assigns each point $\mathbf{p} \in \mathcal{R}^3$ of the transmit array to a polarized vector $\mathbf{x}(\mathbf{p}) \in \mathcal{C}^3$. Similarly, $\mathbf{y}(\cdot)$ is the receive vector field. The system response $\mathbf{C}(\cdot,\cdot)$ is a 3×3 complex integral kernel where its domain is the set of transmit vector fields and its range is the set of receive vector fields. The matrix $\mathbf{C}(\mathbf{q},\mathbf{p})$ gives the channel gain and polarization between the transmit position $\mathbf{p}$ and receive position $\mathbf{q}$. The vector field $\mathbf{z}(\cdot)$ is the additive noise.

The system response can be decomposed into three responses:

$$\mathbf{C}(\mathbf{q},\mathbf{p}) = \iint \mathbf{A}_r(\mathbf{q},\hat{\boldsymbol{\kappa}})\,\mathbf{H}(\hat{\boldsymbol{\kappa}},\hat{\mathbf{k}})\,\mathbf{A}_t(\hat{\mathbf{k}},\mathbf{p})\,d\hat{\mathbf{k}}d\hat{\boldsymbol{\kappa}} \tag{2}$$

where $\mathbf{A}_t(\cdot,\cdot)$, $\mathbf{A}_r(\cdot,\cdot)$ and $\mathbf{H}(\cdot,\cdot)$ are 3×3 complex integral kernels. The *transmit array response* $\mathbf{A}_t(\cdot,\cdot)$ maps the excitation current distribution to the radiated field pattern. Similarly, the *receive array response* $\mathbf{A}_r(\cdot,\cdot)$ maps the incident field pattern to the induced current distribution. The *channel response* $\mathbf{H}(\hat{\boldsymbol{\kappa}},\hat{\mathbf{k}})$ gives the channel gain and polarization between the transmit direction $\hat{\mathbf{k}}$ and receive direction $\hat{\boldsymbol{\kappa}}$ (see Figure 1). We will next model these responses.

2.1 Array Responses

From Maxwell equations, the electric field $\boldsymbol{\mathcal{E}}(\cdot)$ due to the current density $\boldsymbol{\mathcal{J}}(\cdot)$ satisfies [13]

$$\left(-\nabla_{\mathbf{p}} \times \nabla_{\mathbf{p}} \times + k_0^2\right) \boldsymbol{\mathcal{E}}(\mathbf{p}) = \mathrm{i}k_0\eta\boldsymbol{\mathcal{J}}(\mathbf{p})$$

where $k_0 = 2\pi/\lambda$, λ is the wavelength and η is the intrinsic impedance. The inverse map is

$$\boldsymbol{\mathcal{E}}(\mathbf{k}) = \int \boldsymbol{\mathcal{G}}(\mathbf{k},\mathbf{p})\,\boldsymbol{\mathcal{J}}(\mathbf{p})\,d\mathbf{p}$$

for some integral kernel $\boldsymbol{\mathcal{G}}(\cdot,\cdot)$. The kernel $\boldsymbol{\mathcal{G}}(\cdot,\cdot)$ is often referred as the Green function in electromagnetic theory where it is commonly derived with a given coordinate system. As we

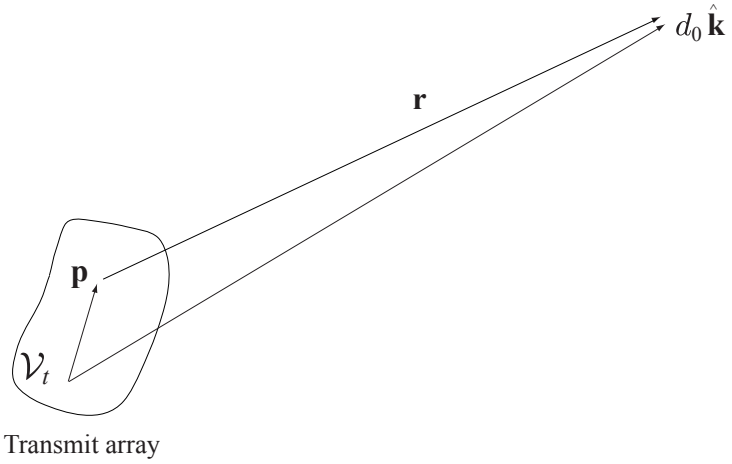

Figure 3: A transmitting continuous array.

want to investigate the effect of array geometry in addition to array size, a coordinate-free version is derived in Appendix A and is given by

$$\boldsymbol{\mathcal{G}}(\mathbf{k},\mathbf{p}) = \frac{\mathrm{i}\eta e^{\mathrm{i}2\pi r/\lambda}}{2\lambda r}\Big[(\mathbf{I}-\hat{\mathbf{r}}\hat{\mathbf{r}}^\dagger) + \frac{\mathrm{i}}{2\pi r/\lambda}(\mathbf{I}-3\hat{\mathbf{r}}\hat{\mathbf{r}}^\dagger) - \frac{1}{(2\pi r/\lambda)^2}(\mathbf{I}-3\hat{\mathbf{r}}\hat{\mathbf{r}}^\dagger)\Big] \tag{3}$$

where $\mathbf{r} = \mathbf{k} - \mathbf{p}$. It has three terms: far-field, intermediate-field and near-field. Only the far-field term corresponds to the radiated field as it falls off inversely as the distance apart r, and hence its power follows the inverse square law. The power of the remaining two terms falls off much faster than r^{-2} (r^{-4} and r^{-6} respectively) so they do not contribute to electromagnetic radiation.

Consequently, the transmit array response is given by

$$\mathbf{A}_t(\hat{\mathbf{k}},\mathbf{p}) = \frac{\mathrm{i}\eta e^{\mathrm{i}2\pi r}}{2\lambda^2 r}\big(\mathbf{I}-\hat{\mathbf{r}}\hat{\mathbf{r}}^\dagger\big), \quad \mathbf{p}\in\mathcal{V}_t \tag{4}$$

and $\mathbf{r} = d_0\hat{\mathbf{k}} - \mathbf{p}$ (see Figure 3) where d_0 is the reference distance and $\mathcal{V}_t$ denotes the transmit space. In the expression, both position vector $\mathbf{p}$ and reference distance d_0 are normalized to a wavelength. The reference distance d_0 is chosen such that $d_0 \gg p$ for all position vector $\mathbf{p}\in\mathcal{V}_t$, the far-field region. Then, we have the following approximations:

$$1/r \approx 1/d_0, \quad r \approx d_0 - \hat{\mathbf{k}}^\dagger\mathbf{p}, \quad \text{and} \quad \hat{\mathbf{r}} \approx \hat{\mathbf{k}}$$

and the array response can be approximated by

$$\mathbf{A}_t(\hat{\mathbf{k}},\mathbf{p}) \approx \frac{\mathrm{i}\eta e^{\mathrm{i}2\pi d_0}}{2\lambda^2 d_0}\big(\mathbf{I}-\hat{\mathbf{k}}\hat{\mathbf{k}}^\dagger\big)\exp(-\mathrm{i}2\pi\hat{\mathbf{k}}^\dagger\mathbf{p}), \quad \mathbf{p}\in\mathcal{V}_t \tag{5}$$

The dyad $\mathbf{I}-\hat{\mathbf{k}}\hat{\mathbf{k}}^\dagger$ is a 3×3 rank 2 matrix and constrains the oscillation direction of the radiated field to be perpendicular to its propagation direction. The propagation term $\exp(-\mathrm{i}2\pi\hat{\mathbf{k}}^\dagger\mathbf{p})$

	Frequency (GHz)	No. of Clusters	Cluster Angle (°)
USC UWB [15]	0 – 3	2 – 5	37
Intel UWB [16]	2 – 8	1 – 4	11 – 17
Spencer [17]	6.75 – 7.25	3 – 5	25.5
COST 259 [18]	24	3 – 5	18.5

Table 1: Summary of indoor spatial channel measurements.

relates the propagation direction $\hat{\mathbf{k}}$ of the radiated field to the excitation position $\mathbf{p}$ on the array. By the reciprocity theorem for antennas [14], the receive array response is

$$\mathbf{A}_r(\mathbf{q}, \hat{\boldsymbol{\kappa}}) \approx \frac{-\mathrm{i}\eta^* e^{-\mathrm{i}2\pi d_0}}{2\lambda^2 d_0} \left(\mathbf{I} - \hat{\boldsymbol{\kappa}}\hat{\boldsymbol{\kappa}}^\dagger\right) \exp(\mathrm{i}2\pi\hat{\boldsymbol{\kappa}}^\dagger\mathbf{q}), \quad \mathbf{q} \in \mathcal{V}_r \tag{6}$$

for all normalized position vector $\mathbf{q}$ of the receive space $\mathcal{V}_r$ and incident field from direction $\hat{\boldsymbol{\kappa}}$.

2.2 Clustered Channel Response

Recent indoor channel measurements show that physical paths are clustered around the transmit and receive directions as illustrated in Figure 1. In indoor environment, clustering can be the result of reflection from walls and ceilings, scattering from furniture, diffraction from door-way openings, and transmission through soft partitions. Table 1 summaries the measurement results in the literature. They show that the number of clusters ranges from 1 to 5, and the cluster azimuth/elevation angles vary from 10° to 30°. In general, the clustering phenomenon occurs when the transmitter-receiver separation is comparable to the size of channel objects and is typical in the indoor and urban environments.

Following the ray-tracing model in [19] and grouping the paths into clusters as in [18], yields the channel response

$$\mathbf{H}(\hat{\boldsymbol{\kappa}}, \hat{\mathbf{k}}) = \frac{1}{\sqrt{N_l}} \sum_{i=1}^{M} \sum_{j \in \mathcal{S}_i} \boldsymbol{\Gamma}_j \delta(\hat{\boldsymbol{\kappa}} - \hat{\boldsymbol{\kappa}}_j) \delta(\hat{\mathbf{k}} - \hat{\mathbf{k}}_j) \tag{7}$$

where $\boldsymbol{\Gamma}_j$ denotes the attenuation and polarization on the jth path, $\mathcal{S}_i$ denotes the set of propagation paths in the ith cluster and N_l is the total number of these paths. The response has the desired property of array-independent; however, there is an arbitrary number of paths in each cluster and hence lessens its analytical tractability. As the channel response is sandwiched between the array responses, a common practice is to smooth out the channel response by the array responses; however, the characteristics of the channel are then mixed up with that of antenna arrays.

Instead, we zoom out the granularity of the channel description and characterize the channel by the set of cluster boundaries. Reference to Figure 1, Ω_t being the union of $\Omega_{t,i}$'s, is the angular interval subtended by the scattering clusters being illuminated by the transmit array. Similarly, Ω_r is the scattering interval as observed from the receive array[1]. Then, the channel response satisfies

$$\mathbf{H}(\hat{\boldsymbol{\kappa}}, \hat{\mathbf{k}}) \neq 0 \quad \text{only if} \quad (\hat{\boldsymbol{\kappa}}, \hat{\mathbf{k}}) \in \Omega_r \times \Omega_t \tag{8}$$

To make sure the well-conditionedness of $\mathbf{H}(\cdot, \cdot)$, we assume that (1) $\int \|\mathbf{H}(\hat{\boldsymbol{\kappa}}, \hat{\mathbf{k}})\|^2 \, d\hat{\boldsymbol{\kappa}} \neq 0$ for all $\hat{\mathbf{k}} \in \Omega_t$ and $\int \|\mathbf{H}(\hat{\boldsymbol{\kappa}}, \hat{\mathbf{k}})\|^2 \, d\hat{\mathbf{k}} \neq 0$ for all $\hat{\boldsymbol{\kappa}} \in \Omega_r$; (2) the point spectrum (set of eigenvalues) of $\mathbf{H}(\cdot, \cdot)$ excluding 0 is infinite; and (3) $\|\mathbf{H}(\hat{\boldsymbol{\kappa}}, \hat{\mathbf{k}})\|^2 \neq 0 \Rightarrow \operatorname{rank}\big(\mathbf{H}(\hat{\boldsymbol{\kappa}}, \hat{\mathbf{k}})\big) = 3$ for all $(\hat{\boldsymbol{\kappa}}, \hat{\mathbf{k}}) \in \Omega_r \times \Omega_t$.

Define the channel solid angles as

$$|\Omega_t| = \int_{\Omega_t} \sin\theta \, d\theta d\phi \quad \text{and} \quad |\Omega_r| = \int_{\Omega_r} \sin\theta \, d\theta d\phi \tag{9}$$

which are the solid angles subtended by the scattering clusters as viewed from the transmitter and receiver respectively. At the transmitter (receiver), $|\Omega_t|$ ($|\Omega_r|$) is the area of projection of the scattering clusters onto the unit sphere enclosing the transmit (receive) array as pictured in Figure 4. For example, in the ideal fully-scattered environment the channel solid angle is 4π, the surface area of a unit sphere.

3 Main Results

Now, the system response in the far-field region can be approximated by

$$\mathbf{C}(\mathbf{q}, \mathbf{p}) \approx \frac{\eta^2}{4\lambda^4 d_0^2} \int_{\Omega_r} \int_{\Omega_t} a^*(\hat{\boldsymbol{\kappa}}, \mathbf{q}) \big(\mathbf{I} - \hat{\boldsymbol{\kappa}}\hat{\boldsymbol{\kappa}}^\dagger\big) \mathbf{H}(\hat{\boldsymbol{\kappa}}, \hat{\mathbf{k}}) \big(\mathbf{I} - \hat{\mathbf{k}}\hat{\mathbf{k}}^\dagger\big) a(\hat{\mathbf{k}}, \mathbf{p}) \, d\hat{\mathbf{k}} d\hat{\boldsymbol{\kappa}}, \ (\mathbf{q}, \mathbf{p}) \in \mathcal{V}_r \times \mathcal{V}_t \tag{10}$$

where

$$a(\hat{\mathbf{k}}, \mathbf{p}) = \exp(-\mathrm{i}2\pi \hat{\mathbf{k}}^\dagger \mathbf{p}) \tag{11}$$

As $\mathbf{H}(\hat{\boldsymbol{\kappa}}, \hat{\mathbf{k}})$ is well-conditioned in $\Omega_r \times \Omega_t$, the spatial degrees of freedom will be constrained by the integral kernels:

$$a^*(\hat{\boldsymbol{\kappa}}, \mathbf{q}) \big(\mathbf{I} - \hat{\boldsymbol{\kappa}}\hat{\boldsymbol{\kappa}}^\dagger\big), \ \ (\hat{\boldsymbol{\kappa}}, \mathbf{q}) \in \Omega_r \times \mathcal{V}_r \quad \text{and} \quad \big(\mathbf{I} - \hat{\mathbf{k}}\hat{\mathbf{k}}^\dagger\big) a(\hat{\mathbf{k}}, \mathbf{p}), \ \ (\hat{\mathbf{k}}, \mathbf{p}) \in \Omega_t \times \mathcal{V}_t$$

For unpolarized antennas, it is equivalent to studying the kernel

$$a(\hat{\mathbf{k}}, \mathbf{p}), \quad (\hat{\mathbf{k}}, \mathbf{p}) \in \Omega \times \mathcal{V} \tag{12}$$

[1]Note that the clusters illuminated by the transmit array need not be the same as those observed from the receive array.

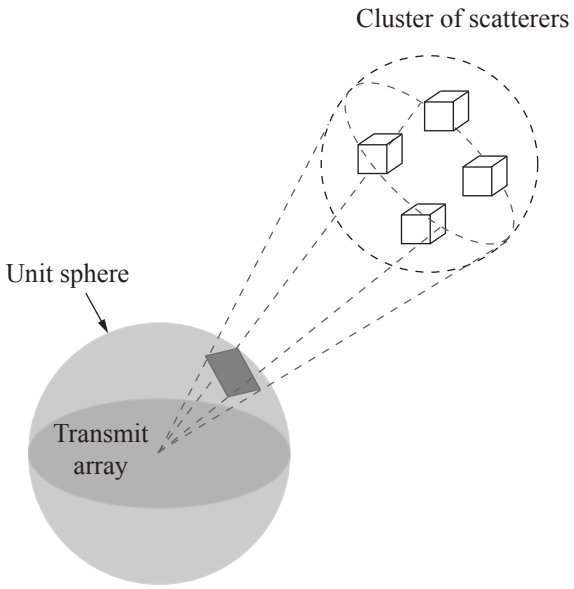

Figure 4: The shaded area on the unit sphere is the channel solid angle subtended by the scattering cluster being illuminated by the transmit array.

where $\mathcal{V}$ can be the transmit or receive spaces, and Ω is the corresponding scattering interval. We consider the following decomposition (equivalent to singular value decomposition on finite-dimensional matrices):

$$a(\hat{\mathbf{k}}, \mathbf{p}) = \sum_n \sigma_n \eta_n(\hat{\mathbf{k}}) \xi_n^*(\mathbf{p}), \quad (\hat{\mathbf{k}}, \mathbf{p}) \in \Omega \times \mathcal{V} \tag{13}$$

where $\{\sigma_n\}$ is a sequence of non-negative numbers (singular values), and $\{\eta_n(\cdot)\}$ and $\{\xi_n(\cdot)\}$ are orthonormal sets satisfying

$$\int_\Omega \eta_n(\hat{\mathbf{k}}) \eta_m^*(\hat{\mathbf{k}})\, d\hat{\mathbf{k}} = \int_{\mathcal{V}} \xi_n(\mathbf{p}) \xi_m^*(\mathbf{p})\, d\mathbf{p} = \delta_{nm} \tag{14}$$

The σ_n, $\eta_n(\cdot)$ and $\xi_n(\cdot)$ are related by

$$\int a(\hat{\mathbf{k}}, \mathbf{p}) \xi_n(\mathbf{p})\, d\mathbf{p} = \sigma_n \eta(\hat{\mathbf{k}}) \tag{15}$$

The subspace spanned by $\int a(\hat{\mathbf{k}}, \mathbf{p}) \xi_n(\mathbf{p})\, d\mathbf{p}$ for all n corresponding to significant σ_n's, gives the set of radiated field patterns that are array-limited to $\mathcal{V}$ and approximately wavevector-limited to Ω. The number of significant singular values gives the dimension of this subspace. The minimum of the dimensions of the transmit and receive subspaces yields the spatial degrees of freedom for unpolarized antennas. For polarized antennas, we consider the 3×3 integral kernel

$$\left(\mathbf{I} - \hat{\mathbf{k}}\hat{\mathbf{k}}^\dagger\right) a(\hat{\mathbf{k}}, \mathbf{p}), \quad (\hat{\mathbf{k}}, \mathbf{p}) \in \Omega \times \mathcal{V} \tag{16}$$

instead. To ease the understanding, we consider linear arrays first, then followed by circular and spherical arrays.

3.1 Unpolarized Linear Arrays

In spherical coordinates, the propagation direction $\hat{\mathbf{k}}$ can be expressed as

$$\hat{\mathbf{k}} = \begin{bmatrix} \sin\theta\cos\phi \\ \sin\theta\sin\phi \\ \cos\theta \end{bmatrix}$$

and $0 \le \theta < \pi$, $0 \le \phi < 2\pi$. Assume Ω is separable over the elevation (θ) and azimuth (ϕ) directions, that is, $\Omega = \Theta \times \Phi$. Consider a linear array of length $2L$ oriented along the z-axis and centered at the origin. Then, the integral kernel $a(\cdot,\cdot)$ in Equation (12) becomes

$$a(\cos\theta, p_{\mathrm{z}}) = \exp(-\mathrm{i}2\pi p_{\mathrm{z}}\cos\theta) \tag{17}$$

and corresponds to the Fourier transform, same as the mapping between the time and frequency domains in waveform channels.

In waveform channels, transmitted signals will be first bandlimited to $[-W, W]$ and then time-limited to $[-T/2, T/2]$. If $s(t)$ is the transmitted signal, then the received signal will be

$$r(t) = \begin{cases} \int_{-W}^{W} \exp(\mathrm{i}2\pi ft) S(f)\, df, & t \in [-T/2, T/2] \\ 0, & \text{otherwise} \end{cases}$$

where $S(f)$ is the Fourier transform of $s(t)$. This operation is equivalent to that performed by the kernel

$$\exp(-\mathrm{i}2\pi ft), \quad (t,f) \in [-T/2, T/2] \times [-W, W] \tag{18}$$

It can be decomposed into a sum of shifted sinc dyads

$$\exp(-\mathrm{i}2\pi ft) = \sum_{n=-\infty}^{\infty} \operatorname{sinc}\Big[2W\big(t - \frac{n}{2W}\big)\Big] e^{-\mathrm{i}\pi nf/W}, \quad (t,f) \in [-T/2, T/2] \times [-W, W] \tag{19}$$

As most of the energy of the sinc function is concentrated within $\pm 1/2W$, so when $T \gg 1/(2W)$, we can make the following approximations:

$$\exp(-\mathrm{i}2\pi ft) \approx \sum_{n=-WT}^{WT} \operatorname{sinc}\Big[2W\big(t - \frac{n}{2W}\big)\Big] e^{-\mathrm{i}\pi nf/W}, \quad (t,f) \in [-T/2, T/2] \times [-W, W] \tag{20}$$

and

$$\int_{-T/2}^{T/2} 2W \operatorname{sinc}\Big[2W\big(t - \frac{n}{2W}\big)\Big] \operatorname{sinc}\Big[2W\big(t - \frac{m}{2W}\big)\Big] dt \approx \delta_{nm}, \quad |n|, |m| \le WT \tag{21}$$

Compared to the decomposition defined in Equation (13)–(14), the number of significant singular values is $2WT$ for $WT \gg 1$. The subspace spanned by

$$\left\{ \sqrt{2W}\,\mathrm{sinc}\Big[2W\big(t - \frac{n}{2W}\big)\Big] : n = 0, \cdots, \pm WT \right\} \tag{22}$$

gives the set of frequency-limited and approximately time-limited waveforms. Cast onto the integral kernel for linear arrays, yields

$$a(\cos\theta, p_z) = \sum_{n=-\infty}^{\infty} \mathrm{sinc}\Big[2L\big(\cos\theta - \frac{n}{2L}\big)\Big]\, e^{-\mathrm{i}\pi n p_z/L}, \quad (\cos\theta, p_z) \in \Omega_\theta \times [-L, L] \tag{23}$$

where $\Omega_\theta = \big\{\cos\theta : \theta \in \Theta\big\}$. The array-limited sinc functions have a resolution of $1/(2L)$ over Ω_θ. Therefore, the dimension of the array-limited and approximately wavevector-limited subspace is $2L|\Omega_\theta|$ for $L|\Omega_\theta| \gg 1$.

Now, we justify the approximation made in Equation (20)–(21), and hence justify the $2L|\Omega_\theta|$ formula. Slepian et al. [20, 21, 22] showed that the integral kernel for waveform channels (Equation (18)) can be decomposed into

$$\exp(-\mathrm{i}2\pi f t) = \sum_{n=0}^{\infty} \sigma_n \varphi_n(t) \Psi_n(f), \quad (t, f) \in [-T/2, T/2] \times [-W, W]$$

and the orthonormal sets $\big\{\varphi_n(\cdot)\big\}$ and $\big\{\Psi_n(\cdot)\big\}$ are the prolate spheroidal wave functions. The frequency-limited function $\Psi_n(\cdot)$ satisfies

$$\int_{-W}^{W} \Psi_n(f)\Psi_m^*(f)\, df = \delta_{nm}, \quad \text{and} \quad \int_{-T/2}^{T/2} \psi_n(t)\psi_m^*(t)\, dt = \sigma_n^2 \delta_{nm}$$

where $\psi_n(\cdot)$ is the inverse Fourier transform of $\Psi_n(\cdot)$. Therefore, $\Psi_n(\cdot)$ contains σ_n^2 of its energy within the time interval $[-T/2, T/2]$. Thus, the behavior of σ_n with n ($1 > \sigma_0 > \sigma_1 > \cdots \geq 0$) determines the dimension of the subspace of frequency-limited and approximately time-limited waveforms. Slepian et al. have shown that when $n \ll 2WT$, σ_n^2 closes to 1; and when $n \gg 2WT$, σ_n^2 closes to 0. The transition occurs in an interval of n centered at $2WT$ with width growing at rate $\ln(2WT)$. Therefore, the dimension of the subspace should be

$$2WT + c_1 \ln(2WT) + o\big(\ln(2WT)\big) \tag{24}$$

for $WT \gg 1$, and c_1 is a constant. Cast onto linear arrays, when Ω_θ contains a single interval, the dimension of the array-limited and approximately wavevector-limited subspace is

$$2L|\Omega_\theta| + c_1 \ln(2L|\Omega_\theta|) + o\big(\ln(2L|\Omega_\theta|)\big) \tag{25}$$

for $L|\Omega_\theta| \gg 1$. However, Ω_θ likely contains more than one interval (see Table 1). Fortunately, Landau et al. [23] showed that when Ω_θ contains M sub-intervals, the dimension is simply

$$2L|\Omega_\theta| + c_2 M \ln(2L|\Omega_\theta|) + o\big(\ln(2L|\Omega_\theta|)\big) \tag{26}$$

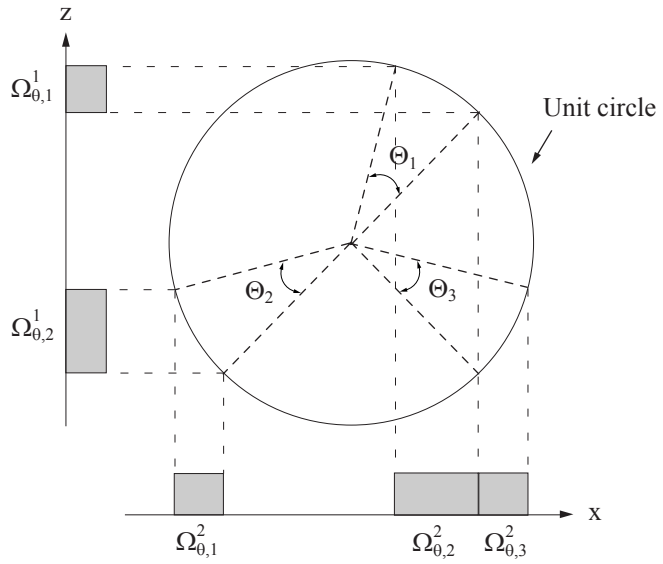

Figure 5: Illustrate the dependence of $|\Omega_\theta|$ on the orientation of a linear array. For a fixed scattering environment with $\Theta = \Theta_1 \cup \Theta_2 \cup \Theta_3$, $|\Omega_\theta|$ is $|\Omega^1_{\theta,1}| + |\Omega^1_{\theta,2}|$ when the array is oriented along the z-axis, and becomes $|\Omega^2_{\theta,1}| + |\Omega^2_{\theta,2}| + |\Omega^2_{\theta,3}|$ when the array is oriented along the x-axis.

for $L|\Omega_\theta| \gg 1$, and c_2 is a constant. Consequently, the dimension of the subspaces heuristically derived based on resolvability agrees in first order with this mathematically more rigorous approach.

3.2 Unpolarized Circular Arrays

Suppose Θ contain a single interval. If the linear array is oriented such that the scattering cluster is at the broadside, then

$$|\Omega_\theta| = \int_\Theta d\cos\theta \approx \int_\Theta d\theta = |\Theta|$$

On the other extreme, if the scattering cluster is at the endfire, then

$$|\Omega_\theta| \approx \int_\Theta \theta\, d\theta = \frac{1}{2}|\Theta|^2$$

As a result, the spatial degrees of freedom depends on the orientation of the linear array in addition to its size and the scattering of physical environment. Figure 5 further illustrates this dependence for Θ containing multiple sub-intervals. To achieve a viable separation of array and channel characteristics, circular arrays are considered next.

Consider a circular array lying on the xy-plane of radius R normalized to a wavelength.

Expressing the position vector $\mathbf{p}$ in spherical coordinates

$$\mathbf{p} = R \begin{bmatrix} \sin\theta' \cos\phi' \\ \sin\theta' \sin\phi' \\ \cos\theta' \end{bmatrix}$$

and $0 \leq \theta' < \pi$, $0 \leq \phi' < 2\pi$, the integral kernel in Equation (12) becomes

$$a(\phi, \phi') = \exp\big[-\mathrm{i}2\pi R \cos(\phi - \phi')\big], \quad \phi \in \Phi \tag{27}$$

As $e^{\mathrm{i}z\cos\phi} = \sum_{n=-\infty}^{\infty} \mathrm{i}^n J_n(z) e^{\mathrm{i}n\phi}$ where $J_n(\cdot)$ is the nth order Bessel function of the first kind (referred as the Jacobi-Anger expansion [24]), it yields

$$a(\phi, \phi') = \sum_{n=-\infty}^{\infty} \mathrm{i}^n J_n(2\pi R)\, e^{\mathrm{i}n\phi} e^{-\mathrm{i}n\phi'}, \quad \phi \in \Phi \tag{28}$$

Obviously, the set $\big\{\frac{1}{\sqrt{2\pi}} e^{\mathrm{i}n\phi'}\big\}$ is orthonromal. If $\Phi = [0, 2\pi)$ (fully-scattered in the azimuth direction), the set $\big\{\frac{1}{\sqrt{2\pi}} e^{\mathrm{i}n\phi}, \phi \in \Phi\big\}$ is orthonormal as well and the expansion in Equation (28) corresponds to the decomposition defined in Equation (13)–(14). Furthermore, when $R \gg 1$, $J_n(2\pi R) \approx 0$ for $|n| > 2\pi R$ [25]. Therefore, the dimension of the array-limited and approximately wavevector limited subspace is $4\pi R$ for $R \gg 1$ and $\Phi = [0, 2\pi)$.

When $\Phi \subset [0, 2\pi)$, the set $\big\{e^{\mathrm{i}n\phi}, \phi \in \Phi\big\}$ is no longer orthogonal. Still, the subspace of array-limited radiated field patterns is spanned by

$$\big\{\tfrac{1}{\sqrt{2\pi}}\, e^{\mathrm{i}n\phi} : n = -2\pi R, \cdots, 2\pi R\big\} \tag{29}$$

for $R \gg 1$. Therefore, finding the number of significant singular values of $a(\phi, \phi')$, $\phi \in \Phi$ is equivalent to finding the dimension of the subspace of functions that are spanned by the set in Equation (29) and contain most of their energy in Φ.

When Φ contains a single interval, Slepian [26] has shown that the subspace of functions spanned by $\big\{e^{\mathrm{i}n\phi}\big\}_{n=0}^{N-1}$ and contained most of their energy within Φ has a dimension of $N|\Phi|/(2\pi)$ for $N \gg 1$. This is also the dimension of the subspace of index-limited and approximately frequency-limited discrete-time sequences. The orthonormal sets is the set of discrete prolate spheriodal wave functions. As a result, the dimension of the array-limited and approximately wavevector-limited subspace would be $4\pi R \cdot |\Phi|/(2\pi) = 2R|\Phi|$ for $R \gg 1$.

When Φ contains more than one sub-interval, we use the heuristic approach based on resolvability. In linear arrays, the radiated field pattern that has the narrowest beam-width is $\mathrm{sinc}(2L\cos\theta)$ and hence, has a resolution of $1/(2L)$ over Ω_θ. For circular arrays, the radiated field pattern (spanned by the set in Equation (29)) that has the narrowest beam-width is given by

$$g(\phi) = \sum_{n=-2\pi R}^{2\pi R} e^{\mathrm{i}n\phi} = \frac{\sin(\pi 2R\phi)}{\sin\phi} \tag{30}$$

which is the periodic sinc (Dirichlet) function. It attains one main lobe at $\phi = 0$ and has zeros at multiples of $1/(2R)$. Therefore, the resolution of circular arrays over Φ is $1/(2R)$. Hence, the dimension of the array-limited and approximately wavevector-limited subspace is $2R|\Phi|$ for $R|\Phi| \gg 1$. Still, $|\Phi|$ depends on the orientation of the plane of the circular array so spherical arrays are considered next.

3.3 Unpolarized Spherical Arrays

Suppose the radius of the spherical array is R normalized to a wavelength. Then, the integral kernel in Equation (12) becomes

$$a(\hat{\mathbf{k}}, \hat{\mathbf{p}}) = \exp\Big\{ -\mathrm{i}2\pi R\big[\sin\theta \sin\theta' \cos(\phi - \phi') + \cos\theta\cos\theta'\big]\Big\}, \quad \hat{\mathbf{k}} \in \Omega \tag{31}$$

As both position vector and propagation direction attain spherical geometries, the kernel can be decomposed into a sum of dyads of spherical harmonics:

$$a(\hat{\mathbf{k}}, \hat{\mathbf{p}}) = 4\pi \sum_{l=0}^{\infty} \sum_{m=-l}^{l} (-\mathrm{i})^l j_l(2\pi R) Y_{lm}(\theta, \phi) Y_{lm}^*(\theta', \phi'), \quad \hat{\mathbf{k}} \in \Omega \tag{32}$$

where $j_l(\cdot)$ is the spherical Bessel function of the first kind and order l. The set of spherical harmonics $\big\{Y_{lm}(\theta, \phi)\big\}$ is a complete orthonormal set on the surface of a unit sphere. The proof is included in Appendix B. When $\Omega = [0, \pi) \times [0, 2\pi)$ (fully scattered in the entire propagation space), the decomposition agrees with that defined in Equation (13)–(14). Furthermore, when $R \gg 1$, $j_l(2\pi R) \approx 0$ for $l > 2\pi R$ [25]. Therefore, the dimension of the array-limited and approximately wavevector-limited subspace is $4\pi^2 R^2$ for $R \gg 1$ and $\Omega = [0, \pi) \times [0, 2\pi)$.

When $\Omega \subset [0, \pi) \times [0, 2\pi)$, the set $\big\{Y_{lm}(\theta, \phi), \hat{\mathbf{k}} \in \Omega\big\}$ is no longer orthogonal. But the subspace of array-limited radiated field patterns is still spanned by

$$\Big\{Y_{lm}(\theta, \phi) : l = 0, 1, \cdots, 2\pi R \text{ and } m = -l, \cdots, l\Big\} \tag{33}$$

for $R \gg 1$. Figure 6 plots $Y_{2m}(\theta, \phi)$ for $m = 0, 1, 2$, in contrast to sinc functions of linear arrays and complex exponentials of circular arrays. Now, we want to find the dimension of the subspace of functions that are spanned by the set defined in Equation (33) and contain most of their energy in Ω. To solve it, we reiterate the heuristic approach based on resolvability.

The spherical harmonics are separable

$$Y_{lm}(\theta, \phi) = c_{lm} P_l^m(\cos\theta)\, e^{\mathrm{i}m\phi}$$

where $c_{lm} = \sqrt{\frac{2l+1}{4\pi}\frac{(l-m)!}{(l+m)!}}$ for normalization and $P_l^m(\cdot)$ is the associated Legendre function. At $\theta = \pi/2$, the radiated field pattern that has the narrowest beam-width in the azimuth

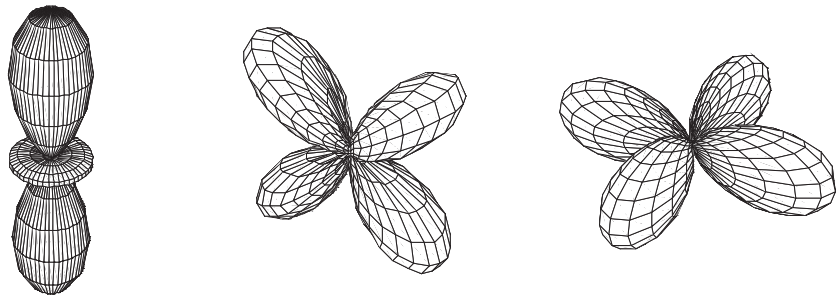

Figure 6: Plots of spherical harmonic functions.

direction, is a linear combination of $Y_{ll}(\pi/2, \phi)$ for $l = 0, \cdots, 2\pi R$ and is given by

$$g_\phi(\phi) = \sum_{l=-2\pi R}^{2\pi R} e^{il\phi} = \frac{\sin(\pi 2R\phi)}{\sin\phi} \tag{34}$$

same as circular arrays of radius R. It attains a main lobe at $\phi = 0$ and has a beam-width of $1/(2R)$. At the main lobe of $g_\phi(\phi)$, the radiated field pattern that has the narrowest beam-width in the elevation direction, is a linear combination of $Y_{2\pi R,m}(\theta, 0)$ for $m = -2\pi R, \cdots, 2\pi R$. Among them, the beam-width around $\theta = \pi/2$ is determined by $Y_{2\pi R,m}(\theta, 0)$ for $m = \pm 2\pi R$ and the corresponding pattern is

$$g_\theta(\theta) = P_{2\pi R}^{2\pi R}(\cos\theta) = \frac{(-1)^{2\pi R}(2\pi R)!}{2^{2\pi R}(2\pi R)!}(\sin\theta)^{2\pi R} \tag{35}$$

Since $\sin^n\theta \approx 1 - n/2(\pi/2 - \theta)^2$ around $\theta = \pi/2$, so the beam-width of $g_\theta(\theta)$ is $4/(2\pi R)$. Hence, the resolution of spherical arrays over Ω is $\frac{1}{2R}\frac{4}{2\pi R}$ equal to $1/(\pi R^2)$. Defining the effective aperture of a spherical array as

$$\mathcal{A} = \pi R^2 \tag{36}$$

which is its area of projection onto a 2-D plane normalized to a square wavelength, the resolution is then expressed as $1/\mathcal{A}$. Consequently, the dimension of the array-limited and approximately wavevector-limited subspace is $\mathcal{A}|\Omega|$ for $\mathcal{A}|\Omega| \gg 1$.

3.4 Wavevector-Aperture-Polarization Product

Suppose $\mathcal{A}_t$ and $\mathcal{A}_r$ denote the effective aperture of the transmit and the receive spherical arrays respectively. Then, the dimensions of the array-limited and approximately wavevector-limited subspace at the transmitter and the receiver are $\mathcal{A}_t|\Omega_t|$ and $\mathcal{A}_r|\Omega_r|$ respectively. The

minimum of them gives the number of spatial degrees of freedom for unpolarized antennas and is equal to

$$\min\big\{\mathcal{A}_t|\Omega_t|,\, \mathcal{A}_r|\Omega_r|\big\} \tag{37}$$

for $\mathcal{A}_t|\Omega_t|, \mathcal{A}_r|\Omega_r| \gg 1$. We refer to this quantity as the *wavevector-aperture product*.

To fully utilize the scattering in physical environments, polarized antennas are need. Now, we consider the 3×3 integral kernel in Equation (16) instead:

$$\big(\mathbf{I} - \hat{\mathbf{k}}\hat{\mathbf{k}}^{\dagger}\big)\, a(\hat{\mathbf{k}}, \mathbf{p}), \quad (\hat{\mathbf{k}}, \mathbf{p}) \in \Omega \times \mathcal{V} \tag{38}$$

This kernel maps the vectored current distribution on the array to the polarized radiated field. The polarization matrix $\big(\mathbf{I} - \hat{\mathbf{k}}\hat{\mathbf{k}}^{\dagger}\big)$ is of rank 2 only. Immaterial to the rank of the channel response $\mathbf{H}(\hat{\boldsymbol{\kappa}}, \hat{\mathbf{k}})$, the rank of the system response can only be equal to or less than 2. Therefore, there is only a 2-fold increase in the dimension of the transmit and receive subspaces, that is, $2\mathcal{A}|\Omega|$ for polarized spherical arrays. Consequently, the number of spatial degrees of freedom is given by

$$\min\big\{2\mathcal{A}_t|\Omega_t|,\, 2\mathcal{A}_r|\Omega_r|\big\} \tag{39}$$

for $\mathcal{A}_t|\Omega_t|, \mathcal{A}_r|\Omega_r| \gg 1$. We refer to this quantity as the *wavevector-aperture-polarization product* which gives the ultimate spatial degrees of freedom.

4 Physical Interpretations and Implications

In this section, we will elucidate the physical insights of the main results, and attempt to bridge between antenna theory and information theory on concepts of antenna arrays.

From Power Gain to Multiplexing Gain

In antenna theory, the channel solid angles determine the amount of transmit power captured by the receiving antennas. The larger the angles are, the more the receiving power is. It is reflected by the path loss exponent commonly used to predict the received signal strength and the range of coverage. But when the size of arrays and/or channel solid angles are substantial, the transmitted power can be splitted up to support parallel data streams. Figure 7 gives a pictorial description on how the antenna array resolves the channel solid angles and creates parallel spatial channels. Thus, the array size and the channel solid angle crucially determine the transition from a pure power gain perspective as in the antenna theory to the spatial multiplexing gain considered in information theory.

Measure of Scattering

The wavevector domain provides an appropriate coordinate to describe the scattering of radio waves by physical objects in the environment. The total solid angles subtended

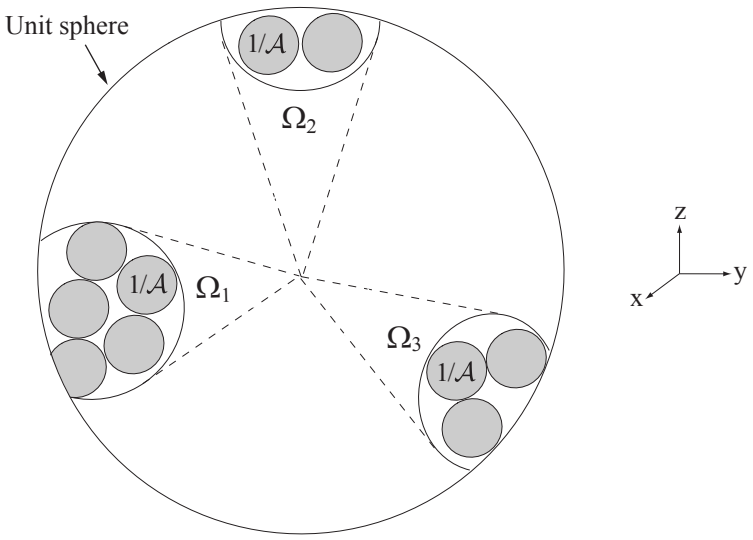

Figure 7: Illustrate the wavevector-aperture product. The shaded circle is of area $1/\mathcal{A}$. The number of these circles used to fill up the channel solid angles gives the spatial degrees of freedom (times a factor of 2 for polarization).

by these objects, $|\Omega_t|$ and $|\Omega_r|$, reflect the amount of channel resources. In the statistical MIMO model, the channel correlation matrix is used to capture these channel resources. The scattering of physical environment is then measured by the rank of this matrix. An inadequate of this measure is its dependence on the number of antennas and their relative positions on the arrays. The channel solid angles, on the other hand, do not depend on these characteristics of antenna arrays (plus array orientation for spherical arrays) and hence provide a more intrinsic measure. Just like delay spread, we would say a typical indoor channel has a delay spread of 10–100 ns without mentioning the bandwidth and/or sampling rate of the system.

Geometry and Size of Arrays

The geometry of antenna arrays determines the appropriate coordinate system to solve the set of Maxwell equations or equivalently, the integral kernel $a(\cdot, \cdot)$ in Equation (12). This results in different mapping between the array and the wavevector domains. The radiated field is then spanned by different basis functions: sinc functions for linear arrays, complex exponentials for circular arrays and spherical harmonics for spherical arrays. The array size determines how many of them are significant or easy to excite. For example, the number of significant excitation modes are $4L$ for linear arrays of length $2L$, $2\pi R$ for circular arrays of radius R and $4\pi\mathcal{A}$ for spherical arrays of effective aperture $\mathcal{A}$. Consequently, given the size of arrays, there is a limit to the number of degrees of freedom. Packing more antennas beyond this limit will not increase the channel capacity significantly even in a fully-scattered

environment.

Polarization Benefits

The polarization benefit is determined by the rank of the system response $\mathbf{C}(\cdot,\cdot)$ in Equation (2) which is the minimum of the rank of the array responses, $\mathbf{A}_r(\cdot,\cdot)$ and $\mathbf{A}_t(\cdot,\cdot)$, and channel response $\mathbf{H}(\cdot,\cdot)$. Therefore, just looking at the rank of the channel response is not sufficient. For example, there is a claim of 6-fold increase in degrees of freedom from polarization [27]. The claim is based on the assumption that the electric field and the magnetic field are oscillating independently, and hence there is a total of 6-fold increase. This independence may hold on the channel response; however, it does not hold in the array responses where the electric field is defined by the curl of the magnetic field. As a result, there is at most 3-fold increase in degrees of freedom. In the intermediate- and near-field regions, the Green function in Equation (3) is of rank 3, so in those two regions the 3-fold increase is attainable. However, in the more important far-field region the rank of the array responses is 2 and hence places a bottleneck on the available degrees of freedom.

The integral kernel for the array response is $\big(\mathbf{I} - \hat{\mathbf{k}}\hat{\mathbf{k}}^{\dagger}\big)\exp(-\mathrm{i}2\pi\hat{\mathbf{k}}\mathbf{p})$ and its physical dimension is 3×3. The polarization benefit is determined by the rank of this kernel, that is, the rank of the polarization matrix $\mathbf{I} - \hat{\mathbf{k}}\hat{\mathbf{k}}^{\dagger}$. It is independent of the physical dimension of the propagation direction $\hat{\mathbf{k}}$. Even the physical dimension of the propagation direction is 1 (equivalent to resolving either the elevation or azimuth directions as in the linear and circular arrays), the rank of the polarization matrix remains 2. This helps us understand better the claim of 4-fold increase in degrees of freedom from polarization [28]. The extra factor of 2 in the claim accounts for the physical dimension of the propagation direction (elevation plus azimuth) which should not be attributed as a polarization benefit.

Effects of Carrier Frequency

The array apertures in the wavevector-aperture-polarization product are normalized quantities. Let $\mathcal{A}_{t0}$ and $\mathcal{A}_{r0}$ denote the absolute effective aperture of the transmit and receive arrays respectively. Then, the number of degrees of freedom can be expressed as

$$\frac{1}{\lambda^2}\,\min\big\{2\mathcal{A}_{t0}|\Omega_t|,\,2\mathcal{A}_{r0}|\Omega_r|\big\} \tag{40}$$

At first glance, the degrees of freedom increases with carrier frequency. Therefore, it is commonly believed that by operating at a higher frequency it is possible to increase the degrees of freedom by packing more antennas on the same wireless device. However, the channel solid angles decrease with increasing frequency. The reasons are twofold: (1) electromagnetic waves of higher frequency attenuate more after passing through or bouncing off channel objects which reduces the number of scattering clusters; and (2) at high frequency the wavelength is small relative to the feature size of typical channel objects, so scattering

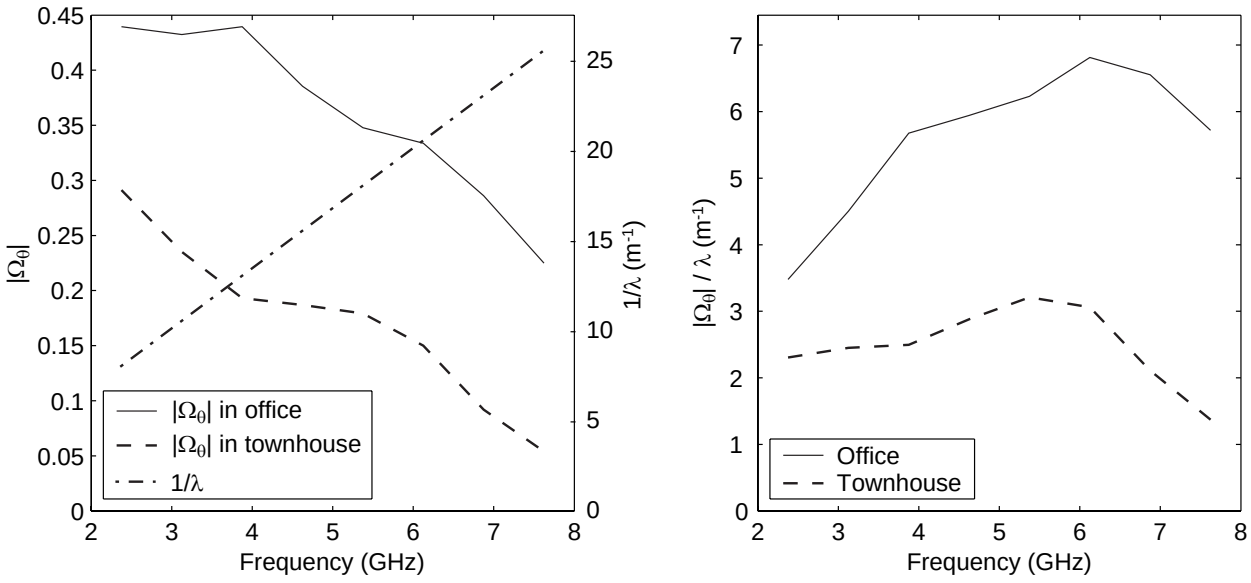

(a) (b)

Figure 8: (a) Reproduce the plot of $|\Omega_\theta|$ versus frequency in an office and residential environments from [16]. (b) Plots the corresponding $|\Omega_\theta|/\lambda$ versus frequency.

appears to be more specular in nature and results in smaller solid angles. These factors together magnify the decrease in the channel solid angles. As a result, it is more conclusive to consider the entities $|\Omega_t|/\lambda^2$ and $|\Omega_r|/\lambda^2$ when judging the performance of multiple-antenna systems in different physical environments and frequency bands.

For example, Figure 8(a) reproduces the measured $|\Omega_\theta|$ at different frequencies reported in [16] where linear arrays were used in the measurement. The $|\Omega_\theta|$ decreases with increasing frequency. As linear arrays can only resolve the elevation direction, we plot the entity $|\Omega_\theta|/\lambda$ in Figure 8(b). The graphs show that $|\Omega_\theta|/\lambda$ initially increase with frequency and after passing the optimal frequencies, then decrease. Interestingly, the optimal frequencies for that particular office and residential environments are between 5 and 6 GHz where the IEEE 802.11a standard is located.

5 Extension to Multiuser Environments

The channel response in Equation (8) is non-zero at transmit direction $\hat{\mathbf{k}}$ and receive direction $\hat{\boldsymbol{\kappa}}$, whenever there is a scatterer providing the connectivity between these directions. In a network, users can be viewed as another type of channel object affecting this connectivity and the wavevector domain provides an appropriate coordinate to describe the physical positions of network users.

Due to the broadcast nature of a wireless channel, signals can be captured and processed by any nearby user. If the user is *cooperative*, it will behave like a scatterer and relay the captured signals to the intended destination. But it can be more sophisticated: it can spatially demodulate the captured signals, then spatially modulate and forward them. Suppose Ω_t^1 and Ω_r^1 are the scattering intervals subtended by the scattering clusters, and Ω_t^i and Ω_r^i $(i = 2, \cdots, K)$ are the scattering intervals subtended by the ith nearby users from the transmitter and the receiver respectively (see Figure 9). Then, the channel response is non-zero only on $\left(\bigcup_{i=1}^K \Omega_r^i\right) \times \left(\bigcup_{i=1}^K \Omega_t^i\right)$. Therefore, the channel solid angles in the wavevector-aperture-polarization product changes from $|\Omega_t^1|$ and $|\Omega_r^1|$ to $\left|\bigcup_{i=1}^K \Omega_t^i\right|$ and $\left|\bigcup_{i=1}^K \Omega_r^i\right|$.

Depending on the extent of overlapping among Ω_t^i's and among Ω_r^i's, they can be totally non-overlapped as in Figure 9(a) or completely overlapped as in Figure 9(b). Except in the later case, the number of spatial degrees of freedom increases with the existence of network users. Consequently, we can think of "relay users" as an additional signal dimension. This is different from the time/frequency counterparts in waveform channels where having multiple users does not provide additional degrees of freedom. They are just sharing the existing time /frequency degrees of freedom.

On the contrary, if the nearby user is *non-cooperative* and interfering, then it will reduce the signal-to-noise ratio on that particular subset of transmit and receive directions. Hence, its effect on the transmitted signal is additive interfering. When $\Omega_r^1 \cap (\bigcup_{i=2}^K \Omega_r^i)$ is non-empty, the receiver can avoid the interferers and abandon this subset of channel resource. This will incur a loss in the receive channel solid angle by $\left|\Omega_r^1 \cap (\bigcup_{i=2}^K \Omega_r^i)\right|$ and hence decrease the spatial degrees of freedom. In the extreme case as shown in Figure 9(b), all the degrees of freedom created by the scatterers will been lost. Furthermore, if the scattering intervals Ω_t and Ω_r are coupled such as in the single-bounce channel, the transmitter should abandon the subset $\Omega_t^1 \cap (\bigcup_{i=2}^K \Omega_t^i)$ as well. This results in a loss of the transmit channel solid angle by $\left|\Omega_t^1 \cap (\bigcup_{i=2}^K \Omega_t^i)\right|$.

6 Optimal Number of Antennas

To ease the understanding, we will use linear arrays as the mapping between the array and wavevector domains is the familiar Fourier transform. For other array geometries, the analysis continues to apply but with different mappings.

6.1 Single-User Channels

When Ω_θ contains a single interval, we can apply the Whittaker-Shannon sampling theorem. Now, $2L|\Omega_\theta|$ number of uniformly-spaced antennas are adequate in the respective transmit

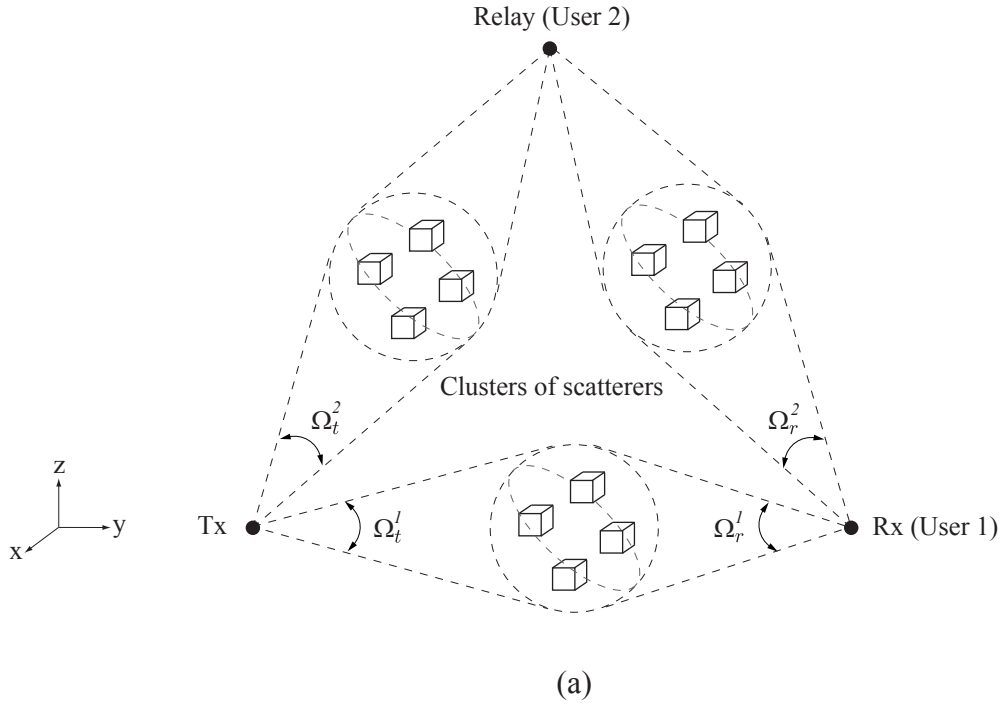

(a)

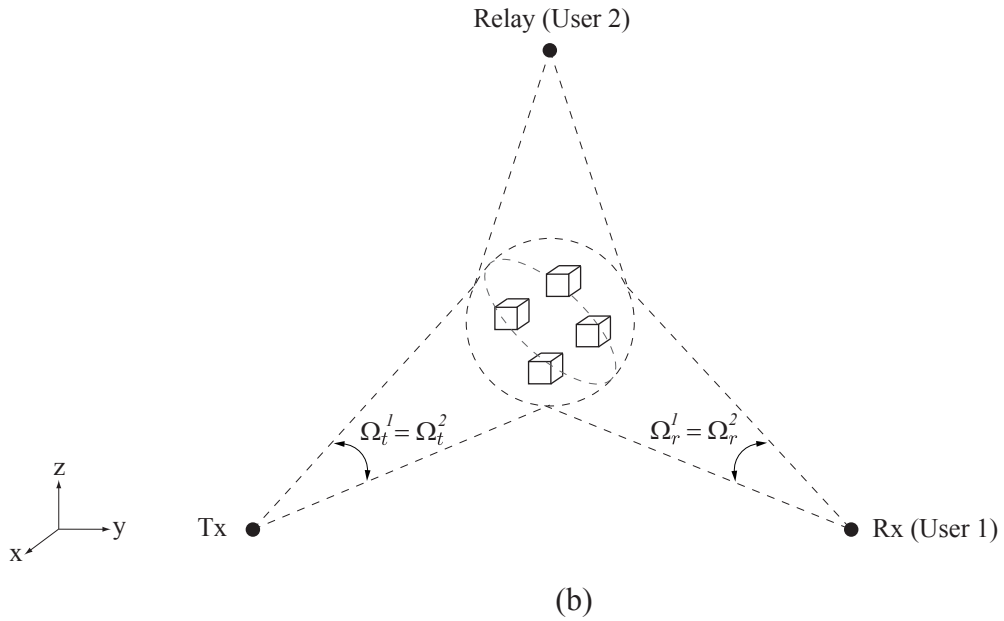

(b)

Figure 9: Illustrates a network with 3 nodes: (a) the channel solid angle subtended by user 2 is non-overlapping with that subtended by the scattering clusters, and (b) the channel solid angle subtended by user 2 exactly overlaps with that of the scattering clusters.

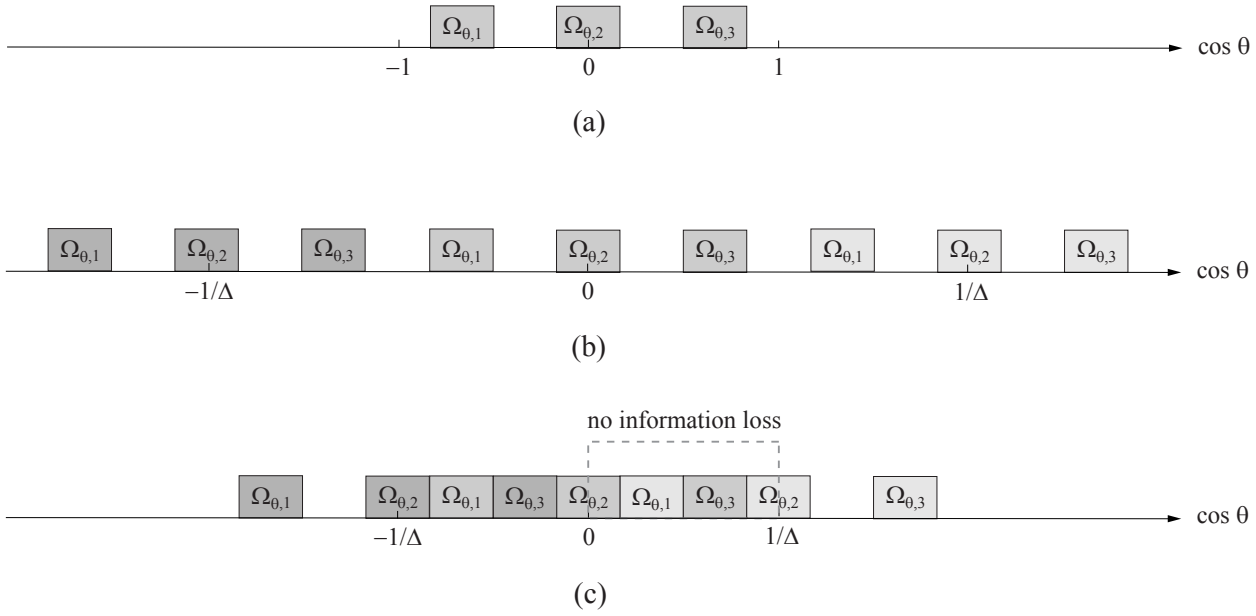

Figure 10: The physical environment with $\Omega_\theta = \Omega_{\theta,1} \cup \Omega_{\theta,2} \cup \Omega_{\theta,3}$ as seen by: (a) a continuous linear array; (b) a discrete linear array with uniform antenna spacing of $\Delta < 1/2$ (normalized to λ); and (c) a discrete linear array with uniform antenna spacing of $\Delta = \frac{1}{|\Omega_\theta|} \geq 1/2$.

and receive spaces. For example, in the fully-scattered environment we have $\Omega_\theta = (-1, 1]$, so $4L$ number of antennas with $\lambda/2$ spacing suffices for optimal performance. Packing more antennas beyond $2L|\Omega_\theta|$ is unnecessary and corresponds to oversampling in the array domain. Putting less antennas, on the other hand, is equivalent to decimating the signal on the array and hence increases the periodicity of the radiated field in the wavevector domain. Grating lobes occurs where the radiated field repeats itself within the interval Ω_θ. At the transmitter, the same information will be sent over more than one direction while at the receiver, signals from different directions will be aliased and perceived as from the same direction.

When Ω_θ contains multiple sub-intervals and is packable without gap[2], $2L|\Omega_\theta|$ number of uniformly-spaced antennas is still adequate as illustrated in Figure 10. When Ω_θ is arbitrary, the problem is equivalent to finding the minimum rate to sample multiband signals[3] with spectral support of $\mathcal{W}$. Landau [29] has derived the lower bound which is $|\mathcal{W}|$, that is, the minumum number of samples taken over a period of T for perfect reconstruction is $T|\mathcal{W}|$. It has been shown that periodic non-uniform sampling can approach this lower bound [30]. This implies that the optimal number of antennas remains $2L|\Omega_\theta|$ but the position of the

[2]There exists α_0 such that translating Ω_θ by multiples of α_0 introduces no overlap, and tiling a number of them covers the entire axis.

[3]Signals have non-vanishing power spectral density over a funite union of arbitrary non-overlapping intervals in the frequency domain.

antennas depends on the structure of Ω_θ.

Averaging over the array orientation, $\mathsf{E}\big[|\Omega_\theta|\big]$ is approximately equal to $\frac{2}{\pi}|\Theta|$. If the parameters, $|\Theta_t|$ and $|\Theta_r|$, in the targeted environment are known a prior, we will demonstrate numerically that the respective $2L\,\mathsf{E}\big[|\Omega_\theta|\big]$ number of uniformly-spaced antennas at the transmitter and the receiver are adequate to approach the optimal ergodic capacity. That is, $\frac{4}{\pi}L_t|\Theta_t|$ number of transmit and $\frac{4}{\pi}L_r|\Theta_r|$ number of receive antennas suffice where $2L_t$ and $2L_r$ are the length of the transmit and receive arrays respectively. This is in analogy to knowing the delay spread in the targeted environment so as to design channel equalizers with the optimal number of taps.

6.2 Multiuser Environments

In a cooperative (relaying) network, simply replacing Ω in the single-user case by $\big|\bigcup_{i=1}^K \Omega_t^i\big|$ at the transmitter and by $\big|\bigcup_{i=1}^K \Omega_r^i\big|$ at the receiver, will give the optimal number of transmit and receive antennas. In a non-cooperative (interfering) network, on the contrary, the performance of any interference management scheme depends on the gaps between the interfering and the desired scattering intervals. Large gaps result in better performance. For example, if $\Omega_{\theta,2}$ in Figure 10(a) corresponds to the interfering interval while $\Omega_{\theta,1}$ and $\Omega_{\theta,3}$ are the desired intervals, increasing the antenna spacing beyond 1/2 (normalized to a wavelength) reduces the gaps between $\Omega_{\theta,2}$ and $\Omega_{\theta,1}$, and between $\Omega_{\theta,2}$ and $\Omega_{\theta,3}$ as illustrated in Figure 10(c). This will degrade the performance. Likewise, decreasing the antenna spacing smaller than 1/2 will not change the gaps (see Figure 10(b)) and hence will not improve the performance. Therefore, the number of antennas in non-cooperative networks is insensitive to the physical environment but depends on the size of arrays.

6.3 Numerical Examples

To verify the results, numerical examples are given. The transmit and receive signals on the arrays are related by

$$y(q_{\rm z}) = \int c(q_{\rm z}, p_{\rm z}) x(p_{\rm z})\, dp_{\rm z} + z(q_{\rm z}) \tag{41}$$

where $z(p_{\rm z})$ is the additive white complex Gaussian noise of zero mean and unit variance. The transmit signal $x(\cdot)$ is normalized such that $\mathsf{E}\big[\|x(p_{\rm z})\|^2\big] = \mathsf{SNR}$. The system response $c(q_{\rm z}, p_{\rm z})$ can be decomposed into

$$c(q_{\rm z}, p_{\rm z}) = \iint e^{{\rm i}2\pi q_{\rm z}\cos\vartheta}\, h(\vartheta,\theta)\, e^{-{\rm i}2\pi p_{\rm z}\cos\theta}\, d\cos\vartheta\, d\cos\theta \tag{42}$$

where θ and ϑ are the transmit and receive angles respectively. We assume that the channel response $h(\vartheta,\theta)$ is uncorrelated at different (ϑ,θ), and is a complex Gaussian random process with zero mean and unit variance within the scattering intervals.

Suppose the antennas are uniformly spaced with separation of Δ_t on the transmit array and Δ_r on the receive array. Then, the (n, m)th element of the channel matrix is given by

$$\mathbf{C}_{nm} = \sqrt{\Delta_r \Delta_t}\, c(n\Delta_r, m\Delta_t) \tag{43}$$

The ergodic capacity with full channel state information at both transmitter and receiver is used for comparison, and is given by

$$\mathsf{E}_{\mathbf{C}}\Big[\sum_i (\log_2 \upsilon\sigma_i^2)^+\Big]$$

where υ satisfies

$$\sum_i (\upsilon - \sigma_i^{-2})^+ = \mathsf{SNR}$$

and σ_i's are the singular values of $\mathbf{C}$.

Two propagation environments will be studied: fully-scattered (ideal) and indoor. In the fully-scattered environment, there are scatterers all around the transmitter and receiver, which result in their respective $|\Omega_\theta|$ being 2. Parameters for the indoor environment are inferred from Table 1. There are 3 scattering clusters each of angle 20° (0.35 rad) randomly placed which result in $\mathsf{E}\big[|\Omega_\theta|\big] \approx \frac{2}{\pi} \times 0.35 \times 3 = 0.67$. Figure 11 plots the channel capacity versus the number of antennas on arrays of 4-wavelength long ($2L = 4$) at SNR of 10 dB. The graphs show that $\big\lceil 2L\, \mathsf{E}[|\Omega_\theta|]\big\rceil$ number of transmit and receive antennas suffice to approach the optimal throughput in both environments. To further re-inforce the observations, Figure 12 plots the channel capacities for different array sizes in the indoor environment. The numbers of transmit and receive antennas in the discrete arrays are kept to be $\big\lceil 2L\, \mathsf{E}[|\Omega_\theta|]\big\rceil$. Continuous arrays are used as upper-bounds for comparison. The graphs show that the channel capacities acheived by the discrete arrays approach closely to those of the continuous arrays.

Taking into account the interfering signals, the additive noise term is no longer white but is colored with the (n, m)th element in the covariance matrix being

$$\delta_{n-m} + \sum_{i=2}^{K} \mathsf{INR}_i \Delta_r \int_{\Theta_r^i} e^{j2\pi \cos\theta \Delta_r (n-m)}\, d\cos\theta \tag{44}$$

where INR_i denotes the average transmit interference-to-noise ratio. Suppose $\mathsf{INR}_i = \mathsf{SNR}$, for $i = 2, \cdots, K$. The scattering intervals Θ_t^i's and Θ_r^i's are assumed to be independently and uniformly distributed over $[0, \pi)$. Figure 13 plots the waterfilling capacity versus the number of receive antennas for discrete arrays of 4-wavelength long at SNR of 10 dB and the number of transmit antennas is fixed to $\big\lceil 2L\, \mathsf{E}[|\Omega_\theta|]\big\rceil = 3$. The graphs show that invariant to the physical environment and the number of interferers, the optimal number of antennas is always $9 = 4L + 1$. Similar obervations are reported when the number of transmit antennas is increased.

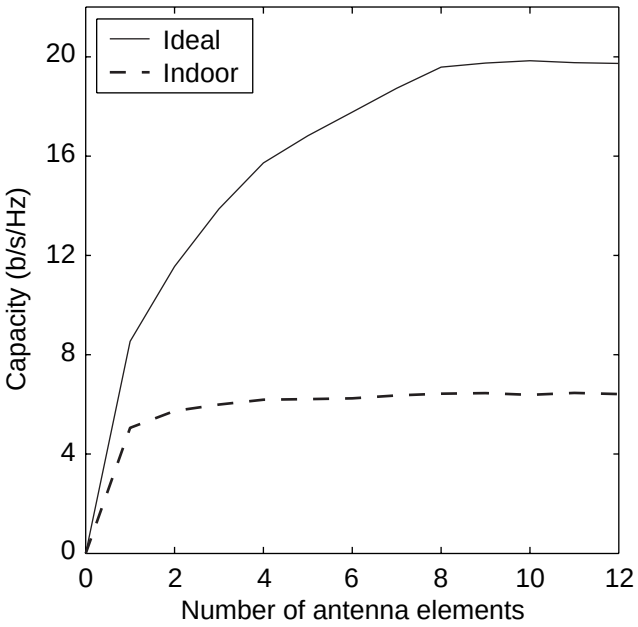

Figure 11: Capacity vs. number of antenna elements for arrays of 4-wavelength long at SNR of 10 dB.

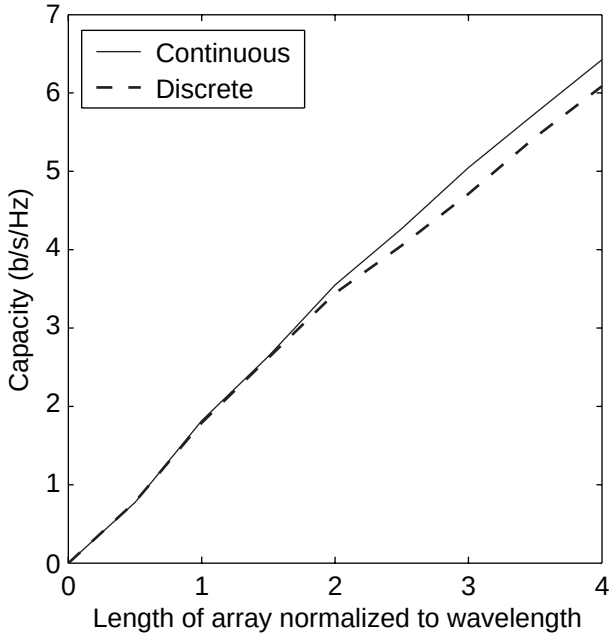

Figure 12: Capacity vs. length of array at SNR of 10 dB in the indoor environment. In the discrete array, the number of transmit and receive antenna elements are both equal to $\lceil 2L\,\mathsf{E}[|\Omega_\theta|]\rceil$.

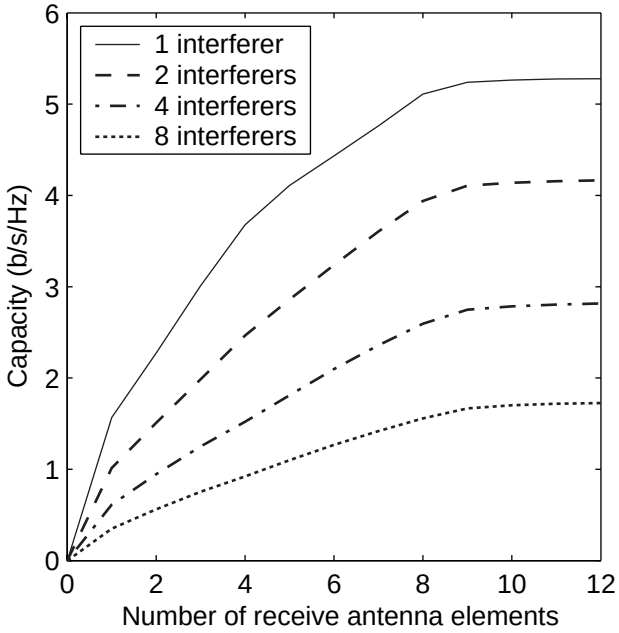

Figure 13: Capacity vs. number of antenna elements vs. number of interferers for arrays of 4-wavelength long at SNR of 10 dB in the indoor environment.

7 Conclusions

Previous studies on the capacity of multiple-antenna channels are based on a statistical MIMO approach. Given a constraint on the areas of the transmit and receive arrays, there is a deterministic limit to the number of spatial degrees of freedom underlying the statistical approach. In this paper, we incorporate antenna theory with observations from spatial channel measurements to obtain a mathematical model. Based on this model, we derive the limit to the spatial degrees of freedom given the space constraints. The results help assess the optimal number of antennas that should be packed on a given wireless device in a given application environment. Nowadays major portion of the chipset for single-antenna systems is occupied by the RF/analog frontend and is expected to increase due to the poor scaling of analog circuitry. Also, most of the power consumption in single-antenna systems goes to the RF/analog frontend. Therefore, optimizing the number of antennas plus RF/analog frontends is practically important for multiple-antenna systems. The proposed mathematical framework would be useful in this aspect.

Acknowledgement

The authors would like to acknowledge the support of the Focus Center Research Program C2S2 of the Microelectronics Advanced Research Corporation (MARCO), DARPA, and the

industrial members of Berkeley Wireless Research Center. In addition, they would like to thank the Intel Research Lab for providing the measurement data plotted in Figure 8(a).

A Proof of Equation (3)

The Green function $\boldsymbol{\mathcal{G}}(\mathbf{p}, \mathbf{p}')$ satisfies

$$\left(-\nabla_{\mathbf{p}} \times \nabla_{\mathbf{p}} \times + k_0^2\right) \boldsymbol{\mathcal{G}}(\mathbf{p}, \mathbf{p}') = \mathrm{i}k_0\eta\, \delta(\mathbf{p} - \mathbf{p}') \tag{45}$$

Notice that under 3-dimensional Fourier transform, the curl operator transforms to

$$\nabla_{\mathbf{p}} \times \stackrel{\mathcal{F}}{\longleftrightarrow} \mathrm{i}\mathbf{k}\times$$

Taking the 3-dimensional Fourier transform with respect to $\mathbf{p}$ on both sides of Equation (45) and applying the following identity,

$$\mathbf{a} \times (\mathbf{b} \times \mathbf{c}) = (\mathbf{a}^\dagger \mathbf{c})\mathbf{b} - (\mathbf{a}^\dagger \mathbf{b})\mathbf{c}\,,$$

we obtain

$$\left[\mathbf{k}\mathbf{k}^\dagger + (k_0^2 - k^2)\mathbf{I}\right]\mathbf{G}(\mathbf{k}, \mathbf{p}') = \mathrm{i}k_0\eta e^{-\mathrm{i}\mathbf{k}^\dagger\mathbf{p}'}$$

Recalling the matrix inversion lemma, the Green function is then given by

$$\mathbf{G}(\mathbf{k}, \mathbf{p}') = \frac{\mathrm{i}\eta}{k_0(k_0^2 - k^2)}(k_0^2\mathbf{I} - \mathbf{k}\mathbf{k}^\dagger)e^{-\mathrm{i}\mathbf{k}^\dagger\mathbf{p}'}$$

Define $\mathbf{r} = \mathbf{p} - \mathbf{p}'$ and perform the inverse Fourier transform result in

$$\boldsymbol{\mathcal{G}}(\mathbf{p}, \mathbf{p}') = \frac{\mathrm{i}\eta}{(2\pi)^3 k_0} \int (k_0^2\mathbf{I} - \mathbf{k}\mathbf{k}^\dagger)\frac{e^{\mathrm{i}\mathbf{k}^\dagger\mathbf{r}}}{k_0^2 - k^2}\, d^3k$$

which is equivalent to

$$\boldsymbol{\mathcal{G}}(\mathbf{p}, \mathbf{p}') = \frac{\mathrm{i}k_0\eta}{(2\pi)^3}\left(\mathbf{I} + \frac{1}{k_0^2}\nabla_{\mathbf{r}}\nabla_{\mathbf{r}}\right) \int \frac{e^{\mathrm{i}\mathbf{k}^\dagger\mathbf{r}}}{k_0^2 - k^2}\, d^3k$$

The integral on the right side is a complex integral and is evaluated as $2\pi^2 e^{\mathrm{i}k_0 r}/r$. Its gradient is

$$\nabla_{\mathbf{r}}\frac{e^{\mathrm{i}k_0 r}}{r} = \left(\mathrm{i}k_0 - \frac{1}{r}\right)\frac{e^{\mathrm{i}k_0 r}}{r}\,\hat{\mathbf{r}}$$

and thus, the second gradient is

$$\nabla_{\mathbf{r}}\nabla_{\mathbf{r}}\frac{e^{\mathrm{i}k_0 r}}{r} = \frac{e^{\mathrm{i}k_0 r}}{r}\left[-k_0^2\hat{\mathbf{r}}\hat{\mathbf{r}}^\dagger + \frac{\mathrm{i}k_0}{r}(\mathbf{I} - 3\hat{\mathbf{r}}\hat{\mathbf{r}}^\dagger) - \frac{1}{r^2}(\mathbf{I} - 3\hat{\mathbf{r}}\hat{\mathbf{r}}^\dagger)\right]$$

Consequently, the Green function is

$$\boldsymbol{\mathcal{G}}(\mathbf{p}, \mathbf{p}') = \frac{\mathrm{i}k_0\eta e^{\mathrm{i}k_0 r}}{4\pi r}\left[(\mathbf{I} - \hat{\mathbf{r}}\hat{\mathbf{r}}^\dagger) + \frac{\mathrm{i}}{k_0 r}(\mathbf{I} - 3\hat{\mathbf{r}}\hat{\mathbf{r}}^\dagger) - \frac{1}{k_0^2 r^2}(\mathbf{I} - 3\hat{\mathbf{r}}\hat{\mathbf{r}}^\dagger)\right]$$

As $k_0 = 2\pi/\lambda$ where λ is the wavelength, so the Green function can also be written as

$$\boldsymbol{\mathcal{G}}(\mathbf{p}, \mathbf{p}') = \frac{\mathrm{i}\eta e^{\mathrm{i}2\pi r/\lambda}}{2\lambda r}\left[(\mathbf{I} - \hat{\mathbf{r}}\hat{\mathbf{r}}^\dagger) + \frac{\mathrm{i}}{2\pi r/\lambda}(\mathbf{I} - 3\hat{\mathbf{r}}\hat{\mathbf{r}}^\dagger) - \frac{1}{(2\pi r/\lambda)^2}(\mathbf{I} - 3\hat{\mathbf{r}}\hat{\mathbf{r}}^\dagger)\right]$$

B Proof of Equation (32)

Define

$$\cos\gamma = \sin\theta\sin\theta'\cos(\phi-\phi') + \cos\theta\cos\theta'$$

in which the argument γ is the angle between the position vector $\mathbf{p}$ and the direction vector $\hat{\mathbf{k}}$. As $-1 \le \cos\gamma \le 1$, so the array response can be expanded in terms of Legendre polynomials which are orthogonal over $[-1, 1]$:

$$e^{-\mathrm{i}2\pi R\cos\gamma} = \sum_{l=1}^{\infty} a_l \sqrt{\frac{2l+1}{2}} P_l(\cos\gamma)$$

The coefficients in this expansion are given by

$$a_l = \sqrt{\frac{2l+1}{2}} \int_{-1}^{1} e^{-\mathrm{i}2\pi Rx} P_l(x)\, dx$$

The Rodrigues formula [25] provides

$$P_l(x) = \frac{1}{2^l l!}\frac{d^l}{dx^l}(x^2-1)^l$$

which results in

$$a_l = \frac{(-1)^l}{2^l l!}\sqrt{\frac{2l+1}{2}} \int_{-1}^{1} (x^2-1)^l \frac{d^l}{dx^l} e^{-\mathrm{i}2\pi Lx}\, dx$$

The integral can be further simplified to

$$\begin{aligned}
\int_{-1}^{1} (x^2-1)^l \frac{d^l}{dx^l} e^{-\mathrm{i}2\pi Rx}\, dx &= (-\mathrm{i}2\pi R)^l \int_{-1}^{1} (x^2-1)^l e^{-\mathrm{i}2\pi Rx}\, dx \\
&= (-\mathrm{i}2\pi R)^l \int_{-1}^{1} (x^2-1)^l \cos(2\pi Rx)\, dx \\
&= (-\mathrm{i}2\pi R)^l \frac{l!}{(-\pi R)^l\sqrt{R}} J_{l+1/2}(2\pi R) \\
&= \mathrm{i}2^{l+1} l!\, j_l(2\pi R)
\end{aligned}$$

and yields

$$a_l = (-\mathrm{i})^l \sqrt{2(2l+1)}\, j_l(2\pi R)$$

Therefore, we obtain

$$e^{-\mathrm{i}2\pi R\cos\gamma} = \sum_{l=0}^{\infty} (-\mathrm{i})^l (2l+1) j_l(2\pi R) P(\cos\gamma)$$

Applying the addition theorem [25], yields

$$e^{-\mathrm{i}2\pi R\cos\gamma} = 4\pi \sum_{l=0}^{\infty}\sum_{m=-l}^{l} (-\mathrm{i})^l j_l(2\pi R) Y_{lm}(\theta,\phi) Y_{lm}^*(\theta',\phi')$$

where $j_l(\cdot)$ is the spherical bessel function of the first kind and lth order.

References

[1] E. Telatar, "Capacity of multi-antenna gaussian channels," *AT&T-Bell Labs Internal Tech. Memo.*, June 1995.

[2] G. J. Foschini and M. J. Gans, "On limits of wireless communications in a fading environment when using multiple antennas," *Wireless Personal Commun.*, vol. 6, pp. 311–35, 1998.

[3] R. G. Gallager, *Information Theory.* Wiley, 1968.

[4] G. J. Foschini, "Layered space-time architecture for wireless communication in a fading environment when using multi-element antennas," *Bell Labs Tech. J.*, pp. 41–59, Autumn 1996.

[5] A. S. Y. Poon, D. N. C. Tse, and R. W. Brodersen, "An adaptive multi-antenna transceiver for slowly flat fading channels," to appear in *IEEE Trans. Commun.*

[6] G. G. Raleigh and J. M. Cioffi, "Spatio-temporal coding for wireless communication," *IEEE Trans. Commun.*, vol. 46, pp. 357–66, Mar. 1998.

[7] A. M. Sayeed, "Deconstructing multi-antenna fading channels," *IEEE Trans. Signal Processing*, vol. 50, pp. 2563–79, Oct. 2002.

[8] K. Liu, R. Vasanthan, and A. M. Sayeed, "Capacity scaling and spectral efficiency in wideband correlated mimo channels," *submitted to IEEE Trans. Inform. Theory.*

[9] A. S. Y. Poon, D. N. C. Tse, and R. W. Brodersen, "Multiple-antenna channels from a combined physical and networking perspective," *Proc. Asilomar Conf. Signals, Systems and Computers*, vol. 2, pp. 1528–32, Nov. 2002.

[10] S. Wei, D. Goeskel, and R. Janaswamy, "On the asymptotic capacity of mimo systems with fixed length antenna arrays," *Proc. ICC*, vol. 4, pp. 2633–37, May 2003.

[11] T. S. Pollock, T. D. Abhayapala, and R. A. Kennedy, "Antenna saturation effects on MIMO capacity," *Proc. ICC*, vol. 4, pp. 2301–05, May 2003.

[12] L. W. Hanlen and M. Fu, "Wireless communications systems with spatial diversity: a volumetric approach," *Proc. ICC*, vol. 4, pp. 2673–77, May 2003.

[13] J. D. Jackson, *Classical Electrodynamics*, 3rd ed. Wiley, 1998.

[14] J. D. Kraus and R. J. Marhefka, *Antennas*, 3rd ed. McGraw-Hill, 2001.

[15] R. J.-M. Cramer, "An evaluation of ultra-wideband propagation channels," Ph.D. dissertation, University of Southern California, Dec. 2000.

[16] A. S. Y. Poon and M. Ho, "Indoor multiple-antenna channel characterization from 2 to 8 GHz," *Proc. IEEE ICC*, vol. 5, pp. 3519–23, May 2003.

[17] Q. H. Spencer *et al.*, "Modeling the statistical time and angle of arrival characteristics of an indoor multipath channel," *IEEE J. Select. Areas Commun.*, vol. 18, pp. 347–60, Mar. 2000.

[18] R. Heddergott and P. Truffer, "Statistical characteristics of indoor radio propagation in NLOS scenarios," Tech. Rep. COST 259 TD(00) 024, Valencia, Spain, Tech. Rep. COST 259, Jan. 2000.

[19] T. Zwick, C. Fischer, and W. Wiesbeck, "A stochastic multipath channel model including path directions for indoor environments," *IEEE J. Select. Areas Commun.*, vol. 20, pp. 1178–92, Aug. 2002.

[20] D. Slepian and H. O. Pollak, "Prolate spheroidal wave functions, fourier analysis and uncertainty - I," *Bell System Tech. J.*, vol. 40, pp. 43–63, Jan. 1961.

[21] H. J. Landau and H. O. Pollak, "Prolate spheroidal wave functions, fourier analysis and uncertainty - II," *Bell System Tech. J.*, vol. 40, pp. 65–84, Jan. 1961.

[22] ——, "Prolate spheroidal wave functions, fourier analysis and uncertainty - III: the dimension of the space of essentially time- and band-limited signals," *Bell System Tech. J.*, vol. 41, pp. 1295–36, July 1962.

[23] H. J. Landau and H. Widom, "Eigenvalue distribution of time and frequency limiting," *J. Mathematical Analysis and Applications*, vol. 77, pp. 469–81, 1980.

[24] M. Abramowitz and I. A. Stegun, *Handbook of Mathematical Functions with Formulas, Graphs, and Mathematical Tables*, 10th ed. New York: Government Printing Office, 1972.

[25] G. Arfken and H. J. Weber, *Mathematical Methods for Physicists*, 4th ed. New York: Academic Press, 1995.

[26] D. Slepian, "Prolate spheroidal wave functions, fourier analysis and uncertainty - V: the discrete case," *Bell Syst. Tech. J.*, vol. 57, pp. 1371–30, May 1978.

[27] M. R. Andrews, P. P. Mitra, and R. deCarvalho, "Tripling the capacity of wireless communications using electromagnetic polarization," *Nature*, vol. 409, pp. 316–18, Jan. 2001.

[28] T. L. Marzetta, "Fundamental limitations on the capacity of wireless links that use polarimetric antenna arrays," *Proc. IEEE ISIT*, p. 51, July 2002.

[29] H. J. Landau, "Necessary density conditions for sampling and interpolation of certain entire functions," *Acta. Math.*, vol. 117, pp. 37–52, Feb. 1967.

[30] C. Herley and P. W. Wong, "Minimum rate sampling and reconstruction of signals with arbitrary frequency support," *IEEE Trans. Inform. Theory*, vol. 45, pp. 1555–64, July 1999.